Spin structures and band gap reduction of high-pressure triple perovskite $Mn_3MnTa_2O_9$.

Elena Solana-Madruga,*[a,] Clemens Ritter,[b] Olivier Mentré[a] and Ángel M. Arévalo-López*[a]

Supplementary Text:

- Experimental Methods:

Room pressure $Mn_4Ta_2O_9$ was prepared as described by Bertaut *et al.* [1]. It was then packed into a Pt capsule and treated under 8 GPa and 1100 ˚C for 20 minutes using the "LEGO" high pressure apparatus in Lille, equipped with a Walker type module. Primary structural characterization was performed using a Cu−$K_{\alpha 1}$ Bruker D8 Advance diffractometer on a Bragg−Brentano geometry in the 5 < 2θ < 90° range.

High resolution neutron diffraction data were accessed at D20 beamline at the Institut Laue-Langevin though EASY-858 experiment (doi: 10.5291/ILL-DATA.EASY-858). Data collection at 300 K for accurate structural characterization was performed using the 90° take-off angle and λ = 1.54 Å in the 0˚ < 2θ < 150˚ angular range with a 0.05˚ step size. Neutron thermodiffraction studies were performed from D20 high intensity data collected at the take-off angle of 42° on ramping from 1.5 to 70 K using λ = 2.41 Å. Magnetic structures were determined from 1.5 K and 40 K long scans collected under the same conditions.

Bulk physical properties were measured using a PPMS 9T Dynacool Quantum Design. Magnetization data were taken in ZFC-FC mode under 1000 Oe and 0.5 T for various sample batches, all showing consistent transitions. Hysteresis loops were measured at several temperatures below, between and above the magnetic transitions. Heat capacity was measured in the 2-300 K temperature range.

UV-VIS reflectance data were collected using a Perkin Elmer Precisely Lambda 650 Spectrometer device, equipped with an STD Detector module & HARRICK Praying Mantis Sampling Kit, scanning the wavelength range 800 - 200 nm in 1 nm steps. Kubelka-Munk analysis were performed considering indirect transition band-gaps. [2] XRD thermodiffraction studies revealing the recovery of the room pressure $Mn_4Ta_2O_9$ polymorph were performed using a Rigaku SmartLab SE 9 kW diffractometer with a Rigaku Reactor X temperature chamber. Diffraction patterns were collected every 20 ˚C from 20 to 800 ˚C in the 5 ˚ < 2θ < 65 ˚ angular region with 0.01 ˚ step size.

All Rietveld refinements for structural and magnetic characterization were performed using FullProf software package and magnetic symmetry analysis using the BasIreps tool implemented in the FullProf suite of programs. [3] The allowed Irreducible representations and their basis vectors are included in Table S1 and the magnetic refined parameters in Table S2. Both magnetic structures follow Irep Γ2, with AFM alignment of the spins along the *c* axis.

- Crystal Structure Determination:

The TPv model of the related $Mn_3MnNb_2O_9$ was used as a starting point for the Rietveld fit of the crystal structure of $Mn_3MnTa_2O_9$. As in the Nb analogue, where NPD and synchrotron X-ray diffraction provide high resolution to determine the *Cc* space group unambiguously. In both cases, the paraelectric *C2/c* symmetry was tested after reconstruction from the refined acentric *Cc* one. This model involves 3, 1 and 5 independent sites for Mn, Ta and O respectively, but it implies Mn3 to lie on a pseudo 2-fold axis, which is far away from the refined *Cc* model. Coherently, worse agreement factors are obtained with R_{WP} = 4.51% for *C2/c* *vs*. 2.25% for *Cc*, supporting the *Cc* symmetry. Superstructure peaks (002), (200) and (110) are labelled in Figure SF1, with [010] and [001] projections of the structural model highlighting their direct relation to the 1:2 Mn:Ta order at the B sites.

- Heat Capacity Analysis:

Fits of the heat capacity data using the Debye-Einstein model for the phonon contribution reveal the magnetic entropy changes occurring at T_N and T_M and the small feature at T_L (Figure S3). They roughly represent the 22(1), 13(1) and 5(1) J/mol K at T_N, T_M and T_L respectively, being ~70% of the theoretical value (4*Rln(2S+1) = 59.59 J/mol K), in line with the results from NPD data.

- **Magnetic Moment Modulation:**

As reported for HP-$Mn_3MnNb_2O_9$,[4] the here presented isostructural TPv $Mn_3MnTa_2O_9$ shows a complex magnetic modulation of the magnetic moments below T_M into a SDW. Figure S4 shows the low temperature magnetic structure as refined from 1.5 K NPD data. Over it, the sinusoidal and UU0DD0-like waves are labelled and the number of frustrated Mn_B-Mn_A magnetic interactions is indicated.

The collinear magnetic structure formed at 40 K describes AFM (101) planes of Mn_A sites, while Mn_B (blue) sites align AFM with Mn1 (black), according to dominant direct d^5-d^5 interactions through octahedral face sharing. [5] This arrangement involves the need for FM interactions between Mn_B and Mn3 (red) / Mn4 (green) A sites, which induces a strong magnetic frustration. The total number of frustrated interactions/ unit cell accounts for a large energy, which can be estimated using a classical spin description as $E_f(k_0) = \Sigma J_{ij}*s_i*s_j$, where J_{ij} is the spin exchange parameter and s_i and s_j are the magnetic moments of i and j sites. Considering a hypothetical AFM non-modulated phase at low temperature with all equivalent magnetic moments of 2.50 μ_B, $E_f(k_0) = 1350*J$.

The low temperature magnetic structure shown in Fig. S4 and following propagation vector $k_L = [⅓ \ 0 \ -⅙]$ shows modulated magnetic moments along the c easy axis, varying between zero and saturated values of 5.1 (1) μ_B. While Mn_A sites remain essentially AFM, with relative sine phase shifts of nearly 1/3 of the nuclear cell, Mn_B site (with a shift ~ 1/6) modulates to minimize the number of frustrated (FM) interactions with all Mn_A sites, which decrease from 12 to 5 FM interactions / cell (dashed blue rectangles in SF4). Therefore, accounting for the 18 cells/magnetic cell and the different magnetic moments in the UU0DD0 waves (4.33 μ_B) and in the sinusoidal waves (5 or 2.5 μ_B), the estimated $E_f(k_L) = 1177.2*J$. The ratio $F = E_f(k_0)/E_f(k_L) = 1.15$, suggests maximum values of 2.2 μ_B/Mn^{2+} would be reached in the hypothetical non-modulated structure to keep the same energy, while the modulation of the magnetic moments allows their partial saturation with averaged moments near 80% of their ideal value. Therefore, the magnetic frustration between A and B sites is confirmed to be the driving force for the modulation of these unusual SDW in A-site manganites with TPv structure.
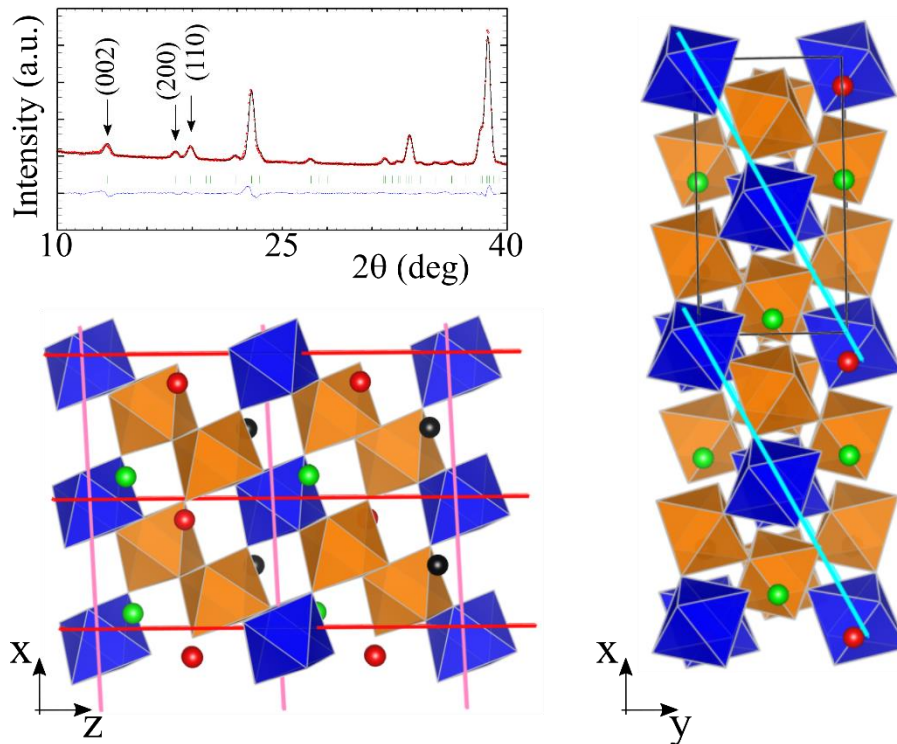

Figure S1. Low angle region of the Rietveld fit against 300 K high resolution NPD data with labelled superstructure peaks (002), (200) and (110) arising from 1:2 Mn:Ta order at the B sites. Structural models of the refined TPv structure of $Mn_3MnTa_2O_9$ with {002}, {200} and {110} lattice planes shown in pink, red and cyan respectively.
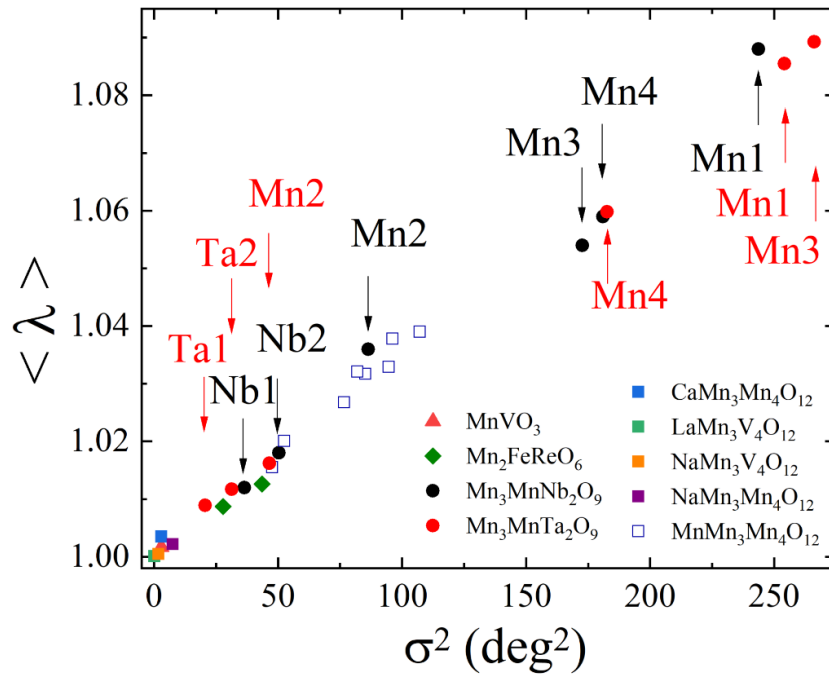
Figure S2. Quadratic elongation / bond angle variance ratio for all cation sites in $Mn_3MnTa_2O_9$ (red labels) compared to those of the B sites in the reference simple ($MnVO_3$),[6] double (Mn_2FeReO_6),[7] and quadruple ($AMn_3B_4O_{12}$)[8-12] perovskites. The distortion of the only isostructural $Mn_3MnNb_2O_9$ TPv [4] are included (black labels). Ta1(Nb1), Ta2(Nb2) and Mn2 sites show comparable distortions to all other values, while those of Mn1, Mn3 and Mn4 sites are much larger, supporting the TPv structure.
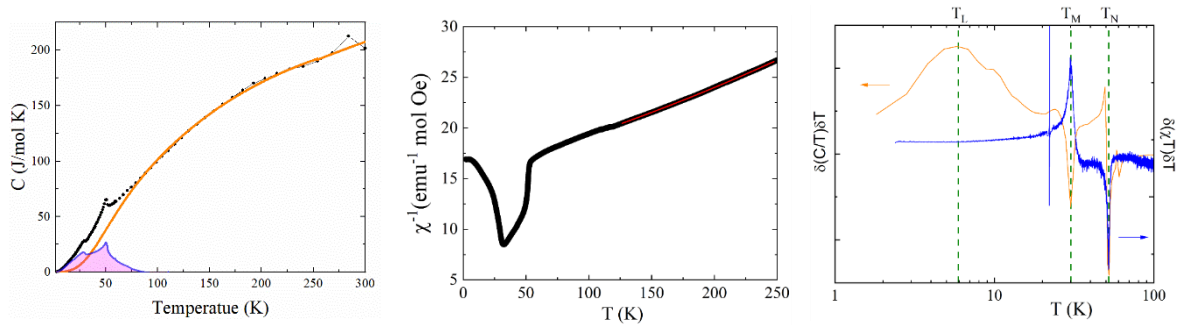

Figure S3. Left panel shows the fit to a Debye-Einstein model (orange line) of the Heat Capacity data along with the magnetic entropy (pink area). Middle panel shows the Curie-Weiss fit (red line) to the paramagnetic region of the inverse magnetic susceptibility of HP-$Mn_3MnTa_2O_9$, measured under 1000 Oe. Right panel shows the derivatives for heat capacity and magnetic susceptibility data for accurate transition temperatures determination.
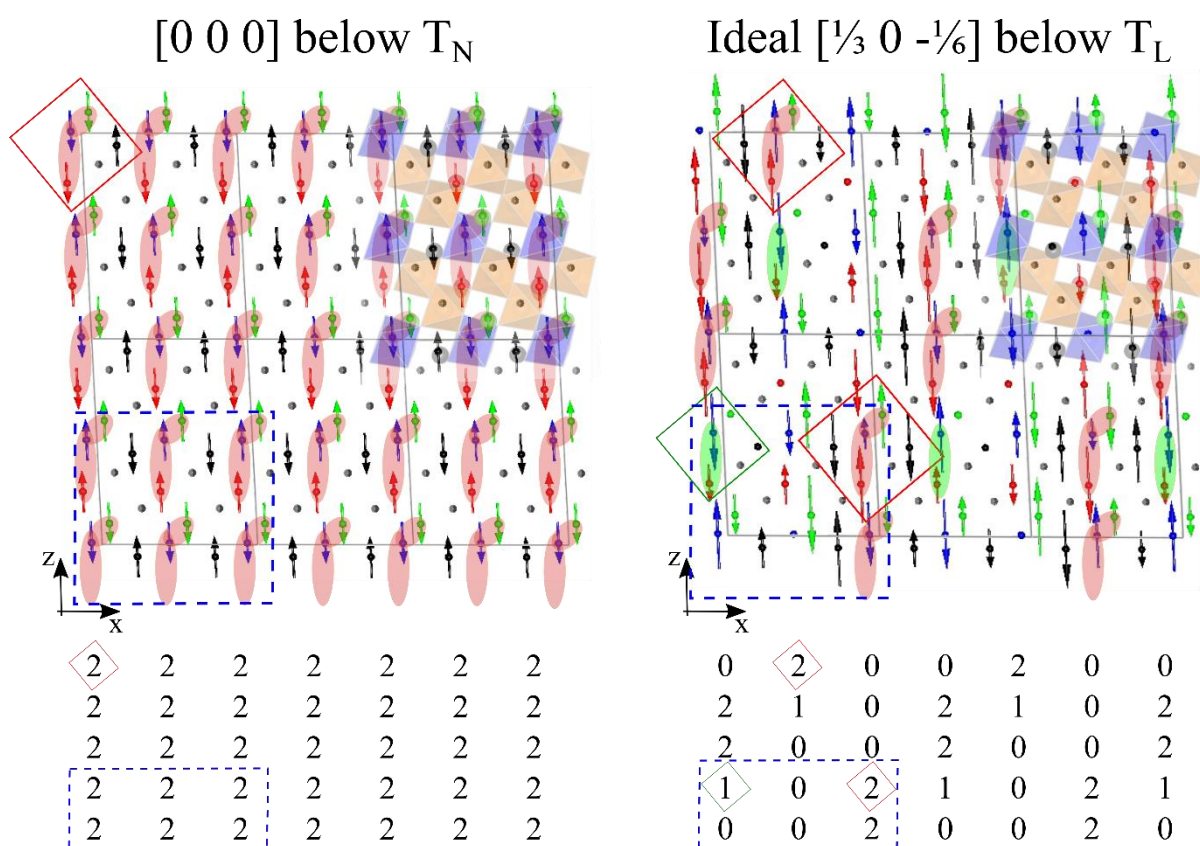
Figure S4. Magnetic structures of the k_0 (left) and k_L (right) phases. Half of the low temperature magnetic cell is shown in both for comparison. Magnetic units identified by the red (or green) squares are shown to have 2 (red shadow), 1 (green shadow) or none (no shadow) frustrated magnetic interactions. Below each panel, the schematic patterns of magnetic frustrated interactions are shown for the same cell size. Blue dashed rectangle identifies the smallest set of asymmetric magnetic units rolling throughout the k_L phase and thus determining the constraint function as detailed in supplementary text.
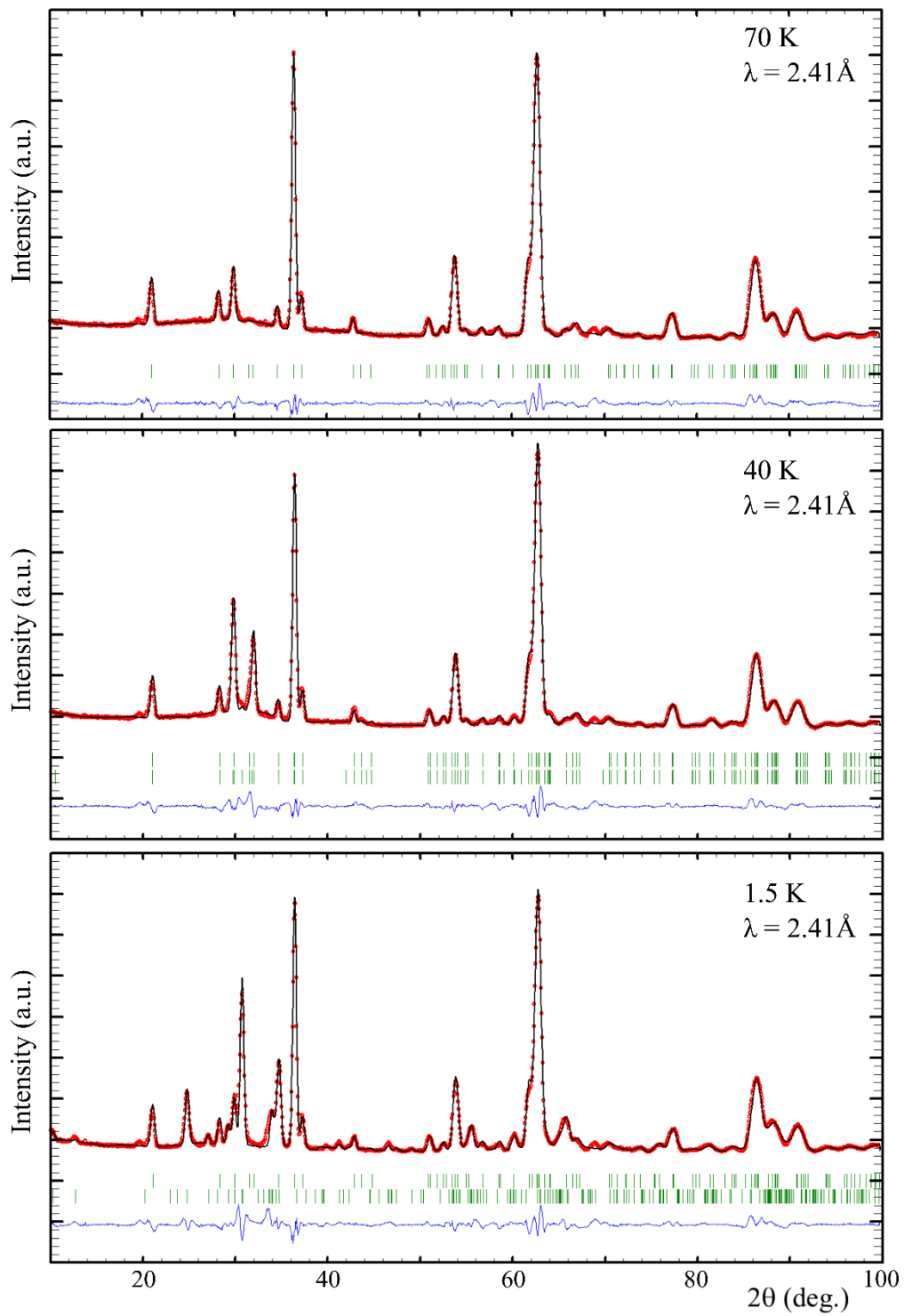
Figure S5. Rietveld fits of the NPD data collected in D20 @ ILL at 70, 40 and 1.5 K using λ = 2.41 Å.
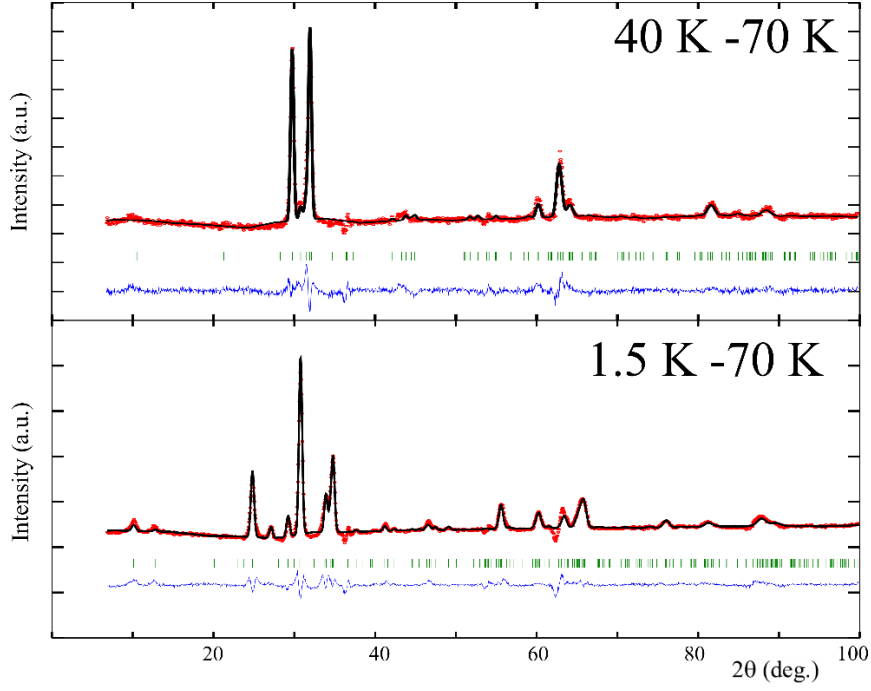
Figure S6. Rietveld fits of the NPD 40 K – 70 K and 1.5 K – 70 K difference patterns using the collinear (a) and SDW (b) magnetic models respectively.

Table S1. Irreducible representations (Irep) and basis vectors (BV) for HP-$Mn_3MnTa_2O_9$ using BasIreps under k_0 = [0 0 0] (top) and k_L = [k_x 0 k_z] (bottom). Upper and lower sets of values for each BV are real and imaginary components respectively.

k_0 = [0 0 0]	Γ_1			Γ_2		
	BV1	BV2	BV3	BV1	BV2	BV3
x y z	1 0 0	0 1 0	0 0 1	1 0 0	0 1 0	0 0 1
	0 0 0	0 0 0	0 0 0	0 0 0	0 0 0	0 0 0
x -y z+1/2	1 0 0	0 -1 0	0 0 1	-1 0 0	0 1 0	0 0 -1
	0 0 0	0 0 0	0 0 1	0 0 0	0 0 0	0 0 0
k_L = [k_x 0 k_z]	Γ_1			Γ_2		
	BV1	BV2	BV3	BV1	BV2	BV3
x y z	2.0757 0 0	0 2.0757 0	0 0 2.0757	2.0757 0 0	0 2.0757 0	0 0 2.0757
	0 0 0	0 0 0	0 0 0	0 0 0	0 0 0	0 0 0
x -y z+1/2	1.819 0 0	0 -1.819 0	0 0 1.819	-1.819 0 0	0 1.819 0	0 0 -1.819
	1 0 0	0 -1 0	0 0 1	-1 0 0	0 1 0	0 0 -1

Table S2. Refined magnetic moments using BV3 of Γ_2 for both magnetic structures. Propagation vector and magnetic phases between different Mn sites are also included for the k_L = [k_x 0 k_z] structure.

	k_0 = [0 0 0]	k_L = [k_x 0 k_z]
μ (μ_B)	2.50(1)	5.1(1)
mphase Mn1	0	-0.375(4)
mphase Mn2	0	-0.151(3)
mphase Mn3	0	0
mphase Mn4	0	-0.388 (4)
k_x	0	0.331(1)
k_z	0	0.848(1)

References

[1]   E. F. Bertaut, L. Corliss, F. Forrat. *J. Phys. Chem. Solids.* **1961**, *21*, 234.

[2]   P. Makuła, M. Pacia, W. Macyk, *J. Phys. Chem. Lett.* **2018**, 9, 6814–6817.

[3]   J. Rodriguez-Carvajal, *Physica B*, **1993**, *192*, 55.

[4]   E. Solana-Madruga, C. Ritter, C. Aguilar-Maldonado, O. Mentré, J. P. Attfield, Á. M. Arévalo-López. *Chem Commun.* **2021**, 57, 8441-8444.

[5]   J. B. Goodenough. *Magnetism and the Chemical Bond*, New Wiley, New York, **1963**, pp. 180-181.

[6]   M. Markkula, A. M. Arevalo-Lopez, A. Kusmartseva, J. A. Rodgers, C. Ritter, H. Wu, J. P. Attfield. Phys. Rev. B, 2011, 84, 094450.

[7]   a) A.M. Arévalo-López, G.M. McNally, J.P. Attfield, Angew. Chem. Int. Ed. 2015, 54, 12074-12077. b) M.R. Li, M. Retuerto, Z. Deng, P.W. Stephens, M. Croft, Q. Huang, H. Wu, X. Deng, G. Kotliar, J. Sánchez-Benítez, J. Hadermann, D. Walker, M. Greenblatt, Angew. Chem. Int. Ed. 2015, 54, 12069-12073.

[8]   A. A. Belik, Y. S. Glazkova, Y. Katsuya, M. Tanaka, A. V. Sobolev, I. A. Presniakov, *J. Phys. Chem. C* **2016**, *120*, 8278–8288

[9]   Y. Shimakawa, S. Zhang, T. Saito, M. W. Lufaso, P. M. Woodward, *Inorg. Chem.* **2014**, *53*, 594–599.

[10]   S. Zhang, T. Saito, M. Mizumaki, W.-T Chen, T. Tohyama, Y. Shimakawa, *J. Am. Chem. Soc.* **2013**, *135*, 6056–6060.

[11]   M. Marezio, P. D.Dernier, J. Chenavas, J. C. Joubert, *J. Solid State Chem.* **1973**, *6*, 16-20.

[12]   S. V. Ovsyannikov, A. M. Abakumov, A. A. Tsirlin, W. Schnelle, R. Egoavil, J. Verbeeck, G. Van Tendeloo, K. V. Glazyrin, M. Hanfland, L. Dubrovinsky. *Angew. Chem. Int. Ed.* **2013**, *52*, 1494-1498.